Molten salt-lithium process induced controllable surface defects in titanium oxide for efficient photocatalysis

Di Zu [a,b], Yiran Ying [a], Zhihang Xu [a], Gao Chen [a], Liqi Bai [a], Safayet Ahmed [a], Zezhou Lin [a], Ye Zhu [a], Ahmed Mortuza Saleque [a], Sixuan She [a], Molly Mengjung Li [a], Md Nahian Al Subri Ivan [a], Hui Wu [b,*], Yuen Hong Tsang [a,*], Haitao Huang [a,*]

[a] *Department of Applied Physics, Hong Kong Polytechnic University, 11 Yucai Road, Kowloon, Hong Kong, China*
[b] *State Key Laboratory of New Ceramics and Fine Processing, School of Materials Science and Engineering, Tsinghua University, Beijing 100084, China*

A B S T R A C T

The efficiency of photoabsorption, photo-generated charge separation, and surface redox reaction determine the overall efficiency of photocatalysts. Therefore, exploring ways to simultaneously optimize the parameters is key to improving the photocatalytic performance. Herein, a novel low-temperature ternary molten salt-lithium reduction method is designed to create controllable oxygen vacancies (Ovs) as well as to manipulate the surface microstructure of the classic photocatalyst TiO_2. The optimized TiO_2 exhibits a 10-fold increase in the photocatalytic RhB breakdown rate and H_2 generation quantity compared to pristine TiO_2. The dual surface defects result in synergistic effects: i) Ovs lower band gap, enhance the charge separation efficiency as capture centers, and facilitate hydrogen adsorption; ii) the enlarged surface area enhances light-harvesting and provides more active sites. This research proposes a novel strategy for manipulating surface defects in a controlled manner and highlights the synergistic optimization of the thermodynamical and kinetical parameters to promote the photocatalytic performance.

1. Introduction

Photocatalysis has been considered as a promising strategy for converting solar energy into chemical energy for fuel production [1–3], environmental purification [4,5], and the inactivation of bacteria and virus [6,7]. Semiconductor-based photocatalysts have emerged as the primary photocatalyst due to their great potential in various applications. Unfortunately, due to the low utilization efficiency of absorbed light and the high recombination of photogenerated carriers, most metal oxide photocatalysts have insufficient photocatalytic efficiency, limiting their performance and greatly impeding their practical applications. The total photocatalytic efficiency (η_{tot}) of a semiconductor relies on its light absorption efficiency (η_{abs}), photo-generated charge separation efficiency (η_{cs}), and surface redox chemical reactions efficiency (η_{redox}), which could be expressed as $\eta_{tot} = \eta_{abs} \times \eta_{cs} \times \eta_{redox}$ [8]. Strong light absorption ability, efficient photo-generated charge separation, and fast surface redox reaction are critical for an ideal photocatalyst.

To address the aforementioned challenges, several strategies, including doping foreign elements [9–11], constructing heterojunctions

[12,13], mesostructuring [14], engineering surface architecture [15], and creating oxygen vacancies (Ovs) [16,17] have been developed to tune the properties of semiconductor photocatalysts and enhance their photocatalytic efficiency. Among these methods, introducing Ovs at the atomic level is a promising way to manipulate the physicochemical properties of metal oxides and optimize their performance. Previous studies suggest that Ovs can change the electronic structure, impact optical absorption feature, and affect adsorption and activation properties in redox reaction [18].

Conventionally, Ovs are implanted in metal oxides by H_2 reduction, which often demands high temperatures and pressure [19]. Chen et al. were the first to report defective TiO_2 by hydrogenating it in a 20 bar H_2 atmosphere at 200 °C for 5 days, resulting in greatly increased photocatalytic activity [20]. However, the high-temperature treatment is cumbersome and energy-intensive. Notably, the high temperature treatment often induces grain growth and phase transformation, which are detrimental to photocatalysis performance. Recently, a lithium reduction method has emerged as a universal strategy for generating defects on the surfaces of a wide variety of simple and complex metal

oxides [21]. However, using lithium as a reductant suffers from a lack of controllability and may even cause safety issues due to its extremely strong reducibility and flammability. Moreover, the solid-state reaction is nonuniform to implant defects in metal oxides. Therefore, despite the versatility of the lithium reduction method to generate defects, it is still challenging to use this method in a safer and more controllable manner.

Herein, we demonstrated a molten salt-lithium reduction method to simultaneously manipulate Ovs and the surface microstructure of a typical semiconductor TiO₂. A ternary molten salt system composed of LiBr, CsBr, and KBr with a low melting point was adopted as a buffer, which significantly reduced the reaction temperature down to 350 ℃ and provided a unique liquid environment for the uniform dispersion of the reactants [22]. The strong polarizing force of the molten salt facilitated the destabilization of Ti-O bonds and promoted the reaction of molten lithium with TiO₂ [23], effectively generating Ovs on TiO₂ nanoparticles. The controllable concentration of Ovs was introduced into TiO₂ by tuning the lithium content. Notably, the surface microstructure of TiO₂ was tailored due to the etching effect of the molten salt-lithium system, resulting in a significantly enlarged surface area. The impact of Ovs and surface microstructure on enhancing photocatalytic performance was clarified using a combination of experimental measurements and theoretical computations. The simultaneous creation of Ovs and enhanced surface area led to a synergistic effect: i) Ovs generate the intermediate gap state and narrow the bandgap, which extend the photoabsorption to the visible light region and increase the number of photo-generated carriers; Also, Ovs act as trap centers to accept e⁻ and change surface charge distribution, thus improving the photo-generated charge separation efficiency and facilitating the hydrogen adsorption, respectively. ii) The enlarged surface area enhances light-harvesting and provides more active sites to facilitate the surface redox reaction kinetics. Therefore, this study paves the way for precisely manipulating surface defects of metal oxides and provides insights into optimizing the three important thermodynamic and kinetic parameters to improve photocatalytic performance synergistically.

2. Experimental part

2.1. Materials

Lithium bromide (LiBr, 99.9%), cesium bromide (CsBr, 99.9%), and potassium bromide (KBr, 99.9%) were purchased from Macklin. TiO₂ (P25) was purchased from Beijing JAH technology Co., Ltd (Beijing, China). Chloroplatinic acid hexahydrate (H₂PtCl₆·6 H₂O, 99.9%) and Rhodamine B (C₂₈H₃₁ClN₂O₃, 99.0%) was purchased from Aladdin. Methanol (CH₃OH), ethanol (C₂H₆O) and hydrochloric acid (HCl) was purchased from Beijing Chemical Reagent Plant (Beijing, China). Lithium was purchased from BEIKE energy technology Co., Ltd (Shenzhen, China).

2.2. Preparation of defective TiO₂

In the glove box (filled with Ar atmosphere), 39.08 wt% LiBr , 42.75 wt% CsBr, and 18.17 wt% KBr weighed 20 g in total were mixed in a quartz beaker. The lithium sheet was 15.6 mm in diameter, 0.25 mm in thickness, and 22 mg in weight. Then, *m* pieces of lithium sheet were put into the quartz beaker (*m*=1, 2, 3). Afterward, the mixture was heated to 350 ℃ for 2 h to melt the lithium fully. 80 mg TiO₂ nanoparticles (P25, degauss) were added to the quartz beaker. After stirring TiO₂ nanoparticles to make them disperse uniformly, the quartz beaker was heated at 350 ℃ for 20 min. Then, the mixture was removed from the glove box. The samples in the quartz beaker were washed with deionized water and ethanol to remove the bromide and residual lithium. Followed by washing with 0.5 M HCl , deionized water, and ethanol with sonication to obtain defective TiO₂ nanoparticles, denoted as TiO₂-*m*. Finally, all the samples were dried in the oven at 60 ℃ for further characterization.

2.3. Characterization

The crystal structure of the materials was identified by X-ray diffraction (XRD) on an X-ray diffractometer (D max-2500, Rigaku, Tokyo, Japan) with Cu Kα irradiation. UV–Vis diffuse reflectance spectra (UV–Vis DRS) were obtained from a Shimadzu UV-3600 spectrometer with BaSO₄ as a reference to characterize the absorbance spectra of TiO₂. X-ray photoelectron spectra (XPS) were collected by X-ray photoelectron spectrometry (Escalab 250Xi, Thermos Fisher Scientific MA, USA) with monochromatic Al Kα (150 W). Using the binding energy of a C 1 s peak of the substrate (284.8 eV), the collected data could be corrected to eliminate the charging effect. Spectral deconvolution was carried out based on the Voigt function convoluting the Gaussian and Lorentzian functions. Electron paramagnetic resonance spectra (EPR) were measured on paramagnetic resonance spectroscopy (FA-200, JEOL) at 300 K. Transmission electron microscopy (TEM) images were obtained using a JEOL-2010 microscope. Raman spectra were measured on a microscopic confocal Raman spectrometer (LabRAM HR800, HORIBA Jobin Yvon) using a 532 nm laser as the excitation source. A surface area analyzer (QuadraSorb SI, Quantachrome) was adopted to measure N₂ nitrogen adsorption-desorption curves. The magnetic properties were measured on a vibrating sample magnetometer (VSM, Lake Shore-7307). The Ti K-edge x-ray absorption spectroscopy (XAS) measurements were performed at Australian Synchrotron (ANSTO). X-ray absorption spectroscopy (XAS) measurements were carried out at the XAS Beamline at the Australian Synchrotron using a set of liquid nitrogen cooled Si (111) monochromator crystals. The electron beam energy is 3.0 GeV. The sample signals were collected in the transmission mode, and the energy was calibrated using Ti foil. The beam size was about 1×1 mm. The Ti K-edge EXAFS data were processed and analyzed using the standard procedures in Athena software [24]. Theoretical EXAFS data of the R space were calculated by FEFF 9.0 and the cif in Artemis software [25]. The fitting process was conducted based on the k^2-weighted FT-EXAFS, and the k-range was set as 4.0–10.0 Å⁻¹. An R-range of 1.0–4.0 Å was employed, and the R-window function is Hanning. Photoluminescence (PL) spectra and time-resolved photoluminescence spectra (TRPL) were acquired by Edinburgh analytical instruments (FLS920). For the measurement of PL lifetime, the used excitation wavelength (λ_{ex}) was 375 nm. The average lifetime (τ_{Ave}) can be calculated according to:

$$\tau_{Ave} = (A_1\tau_1^2 + A_2\tau_2^2) / (A_1\tau_1 + A_2\tau_2)$$

where τ_i is the lifetime, A_i is the relative intensity.

2.4. RhB adsorption experiment before photocatalytic degradation

As for the RhB adsorption experiment, 30 mg of photocatalytic nanoparticles were dispersed in 30 ml RhB solution (2.5×10^{-5} mol L⁻¹). The adsorption quantity of photocatalysts can be calculated as the follow equation:

$$\text{Adsorption } quantity = \frac{(C_0 - C_t)V}{C_0 W}$$

where C_0 and C_t are the initial and residue concentrations (mg/L) after the adsorption of RhB, respectively; V is the volume of the solution (L); and W is the mass of the adsorbent (mg).

2.5. Photocatalytic RhB degradation measurement

In photocatalytic Rhodamine B (RhB) measurement, RhB (2.5×10^{-5} mol L⁻¹) and TiO₂ nanoparticles (1 mg ml⁻¹) in 30 ml deionized water were ultrasonicated for 30 min, followed by magnetic stirring for 1 h in the dark. Then, the solution was irradiated by simulated solar light (micro solar 300, perfect light, Beijing, China) with a cut filter (400 nm) at the light density of 100 mW cm⁻². The concentration of RhB was

tested by UV-Vis spectrophotometry (UV-2600, Shimadzu). RhB degradation rate R was estimated according to the following equation:

$$R\ (\%) = [(C_0 - C_t)/C_0] \times 100\%$$

The rate constant K was estimated according to the pseudo-first kinetics equation as follows:

$$K = -\ln\left(\frac{C_t}{C_0}\right)\Big/ t$$

where C_0 and C_t denote the RhB dye concentration at the starting time and after irradiating, respectively.

2.6. Photocatalytic H_2 generation measurement

For photocatalytic H_2 generation, firstly, ~1% wt Pt nanoparticles were deposited on TiO_2 nanoparticles via irradiating 0.1 mol $H_2PtCl_6 \cdot 6\ H_2O$ solution under UV light for 1 h. Then, 20 mg pristine or reduced TiO_2 nanoparticles loaded with ~1% wt Pt nanoparticles were mixed with 100 ml methanol-water solution, where the volume of methanol was 20 ml as a sacrificial reagent. Finally, the container was sealed and irradiated by a 300 mW Xe lamp under visible light for 3 h at the light density of 100 mW cm^{-2}. The photocatalysts were continually irradiated for 4 cycles during the hydrogen generation stability test. Hydrogen content was determined by gas chromatography (GC-7920).

2.7. Photoelectrochemical performance measurement

The photoelectrochemical measurements were conducted on an electrochemical workstation (CHI-660D, China). Pt foil, a saturated Ag/AgCl and saturated 0.2 M Na_2SO_4 solution were used as counter, reference electrodes and the electrolyte, respectively. For the preparation of working electrode, 1 mg TiO_2 nanoparticles, 750 μl DI water, 150 μl ethanol and 100 μl Nafion were mixed together. After sonication for 30 min, the slurry was coated onto 1 cm × 1 cm FTO substrate. Then,
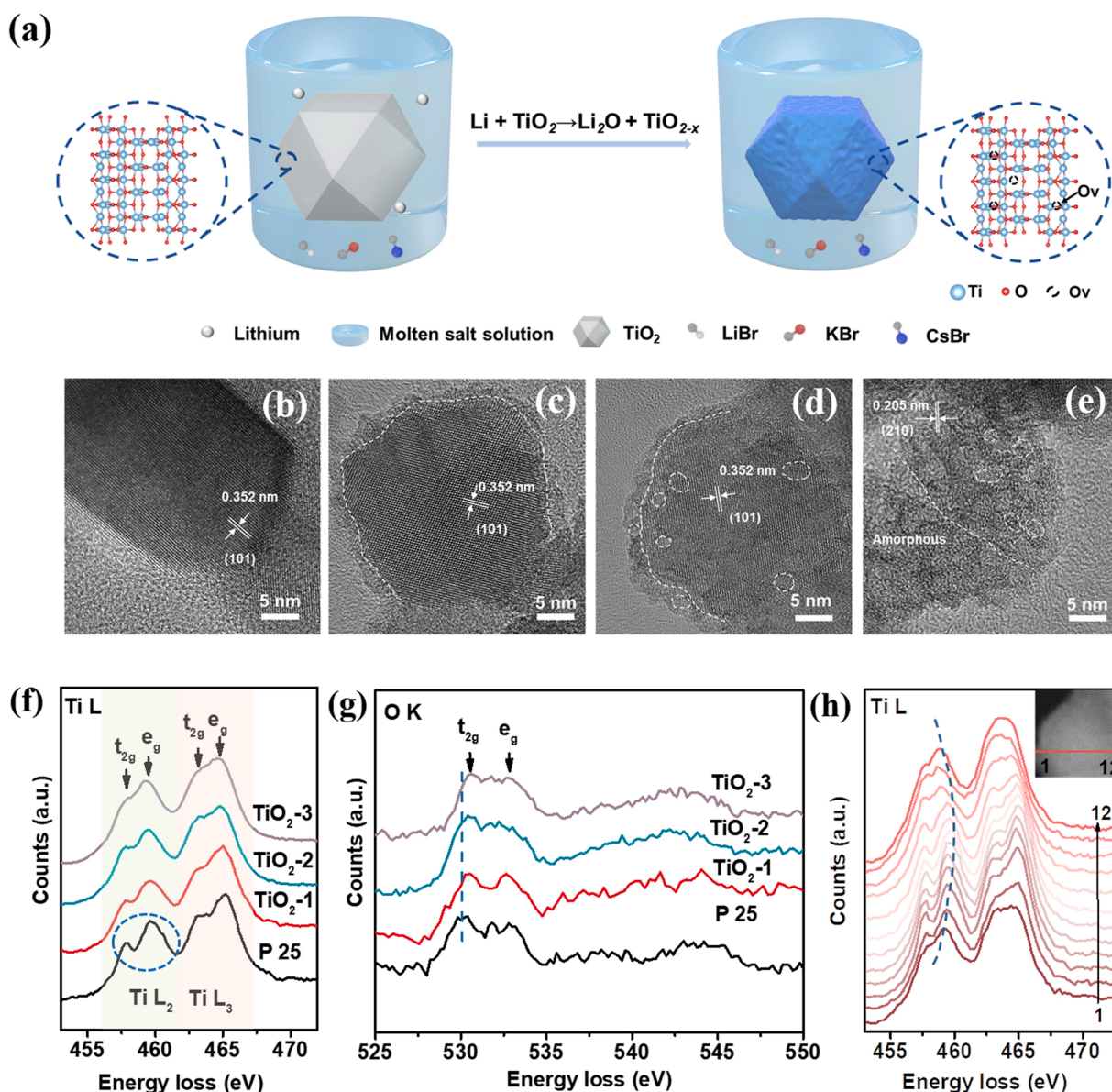

Fig. 1. (a) Schematic illustration of the preparation process of defective TiO_2. HRTEM of (b) pristine TiO_2, (c) TiO_2-1, (d) TiO_2-2 and (e) TiO_2-3. (f) EELS spectra of Ti-L edge and (g) O-K edge of pristine TiO_2 and reduced TiO_2. (h) EELS line-scan spectra of TiO_2-2 with an arrow indicating line-scan direction. Inset is the corresponding STEM image of the TiO_2-2 nanoparticle.

the electrodes were dried at 60 ℃ overnight. Electrochemical impedance spectroscopy (EIS) measurements were carried out at the open circuit potential over the frequency range from 10^{-2} to 10^5 Hz. For the photocurrent-time response test, a 300 W Xe lamp with a cut-off filter (400 nm) was used as the light source. Mott–Schottky plots of TiO_2 electrodes were measured with a frequency of 1 kHz.

The details of DFT calculation can be seen in the Supporting Information.

3. Results and discussion

3.1. Preparation and characterization of TiO₂-Ov

The synthesis procedure of defect engineered TiO_2 is illustrated in Fig. 1a. Typically, the mixture of molten salt (LiBr, CsBr, and KBr) and the reductant lithium was heated at 350 ℃ to fully dissolve the lithium, while lithium exists in the form of liquid droplets and a small portion of bare ions. Then, TiO_2 nanoparticles were added to the solution. The strong polarizing force provided by the molten salt makes the surface of the TiO_2 nanoparticles metastable, and the following reaction occurs.

$$Li + TiO_2 \rightarrow Li_2O + TiO_{2-x}$$
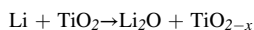
By tuning the lithium content, TiO_2 with different concentrations of Ovs can be obtained, which are denoted as TiO_2-1, TiO_2-2, and TiO_2-3.

High-resolution transmission electron microscopy (HRTEM) shows that pristine TiO_2 possesses high crystallinity with clearly spaced lattice fringes (Fig. 1b). The interplanar spacing is 0.352 nm, corresponding to anatase TiO_2 (101). After the molten salt-lithium treatment, the TiO_2-1 nanoparticle exhibits an obvious core-shell structure (Fig. 1c). The inner part of the TiO_2-1 nanoparticle demonstrates a distinct lattice structure, with a lattice spacing of 0.352 nm, corresponding to the (101) plane of anatase TiO_2. Meanwhile, an amorphous shell layer with a thickness of ~3 nm can be observed surrounding TiO_2-1. HRTEM of TiO_2-2 (Fig. 1d) shows the existence of an amorphous layer (~4 nm) coated on the TiO_2-2 nanoparticles, while the interior of TiO_2-2 nanoparticles is crystallized with *d*-spacing of 0.352 nm, corresponding to (101) planes of anatase TiO_2. Moreover, disordered domains can be created in the TiO_2-2 sample via the molten salt-lithium treatment process, as enclosed by the white dashed lines. TiO_2-3 displays a more obvious surface morphology change (Fig. 1e). Clear lattice fringes with an interlayer spacing of 0.32 nm for (210) crystal plane of rutile TiO_2 can be found in part of the nanoparticle. Besides, pores with a size of ~3 nm and a large area with disordered structure coexist in TiO_2-3, as marked in the HRTEM image. Transmission electron microscopy (TEM) results further confirm that the relatively low temperature of the treatment process can effectively suppress the growth of TiO_2 nanoparticles. The pristine TiO_2 is well dispersed with a particle size of ~25 nm (Fig. S1a). After the molten salt-lithium treatment, the size of TiO_2 nanoparticles remains unchanged (Fig. S1b-d). The type IV curves of N_2 adsorption isotherms (Fig. S2) confirm the existence of mesopores in reduced TiO_2 nanoparticles [26]. The Brunauer–Emmett–Teller surface areas were (S_{BET}) calculated to be 68.46, 73.90, and 95.14 m^2 g^{-1} for TiO_2-1, TiO_2-2, and TiO_2-3, respectively. By contrast, S_{BET} of pristine TiO_2 is only 51.34 m^2 g^{-1}. After the molten salt-lithium treatment process, the surface area shows a distinct increase. Through the molten-salt treatment, the content of mesoporous and disordered structures is found to be increased by increasing the content of lithium. The pore size distributions can be calculated by the density functional theory pore size distribution (NLDFT) model, as displayed in the inset Fig. S2. The surface microstructure of reduced TiO_2 can be calculated and summarized in Table. S1. Electron energy loss spectroscopy (EELS) in Fig. 1f show two doublets are associated with the Ti L_3 edge ($2p_{3/2} \rightarrow 3d$ transition) at a lower energy loss (~457 eV) and the Ti L_2 edge ($2p_{1/2} \rightarrow 3d$ transition) at a higher energy loss (~463 eV), respectively [27,28]. Ti $L_{2,3}$ onset gradually shifts toward lower energy loss with the increase of the reductant

content accompanied by the peak shifting to lower energy, and the peak splitting (denoted by the blue circle in Fig. 1f) becomes less evident in the spectra, which indicates that the oxidation state of Ti decreases. The O-K edge emphasizes the presence of lower oxidation states by the change in intensity ratio and splitting between t_{2g} and e_g (Fig. 1g), indicating that the post-treatment results in Ov gradient into TiO_2 nanoparticles [4,28]. In order to figure out the valence state changes of reduced TiO_2 crystals from the core to the shell, Ti L_2 and L_3 edge EELS spectra across TiO_2-2 crystal were obtained (Fig. 1h). The t_{2g}-e_g crystal-field splitting of Ti $3d$ orbital turns from low resolution at the shell site to higher resolution at the core site, implying that the valence state of Ti at the shell is lower than that at the core. These results indicate that Ov was successfully implanted on the surface of TiO_2 crystals and an Ovs gradient was formed.

X-ray diffraction (XRD) patterns (Fig. 2a) reveal that all the peaks can be well indexed to the anatase phase (JCPDS card no. 71–1166, space group: I41/amd) and rutile phase (JCPDS card no. 21–1276, space group: P42/mnm) for both pristine and reduced TiO_2 nanoparticles [29, 30]. Moreover, no impurities can be identified in TiO_2 after molten salt-lithium treatment. Electron paramagnetic resonance (EPR) is a sensitive characterization method to detect the unpaired electron in the samples (Fig. 2b). Each of the reduced TiO_2 samples shows a symmetrical EPR signal peak at g= 2.002, corresponding to the unpaired electrons at Ov sites [31]. The signal peak area, which is related to the concentration of Ov in samples, is summarized in the inset Fig. 2b. UV-Visible (UV-Vis) diffuse reflectance spectra (DRS) in Fig. S3 show that pristine TiO_2 only absorbs light below 400 nm due to its wide bandgap (3.2 eV). By contrast, reduced TiO_2 extends the photoresponse from UV light to visible regions, indicating enhanced light-harvesting ability due to the introduction of Ovs in TiO_2. The optical photographs (Fig. S4 and S5) show that the color of TiO_2 samples turns from white to dark blue after the molten salt-lithium treatment. The blue color is correlated with the Ti^{3+} as "color centers" in reduced TiO_2 [32]. It is remarkable that the color of reduced TiO_2 is gradually deepened as the amount of reducing agent increases. Ti 2p XPS patterns of pristine TiO_2 (Fig. 2c) show two peaks at 458.6 eV and 464.3 eV, corresponding to Ti $2p_{3/2}$ and Ti $2p_{1/2}$ of Ti^{4+}, respectively. Compared with pristine TiO_2, TiO_2-1, TiO_2-2, and TiO_2-3 show shifts of XPS peaks to lower binding energy by about 0.10, 0.14, and 0.16 eV, respectively. This red shift results from the presence of Ti ions with a low valence state in TiO_2 [33]. It can be proposed that during the molten salt-lithium treatment process, Ovs were generated in the lattice, which was accompanied by the formation of Ti^{3+}, and resulted in the peak shift to the lower binding energy. It can also be concluded from Ti 2p XPS that with the increment of the reductant, the concentration of Ti^{3+} increases correspondingly. The O 1 s XPS spectra of pristine TiO_2 exhibit three fitting peaks (Fig. 2d), where the peak located at 530.0 eV can be attributed to the Ti–O bond (lattice O), and the peak at 531.2 eV is deemed as the O atoms near the Ov (defect O), and the peak centered at 532.2 eV is ascribed to O-H bond (adsorbed O) [18,34]. The concentration of oxygen atoms with different bonding states on the surface of TiO_2 is correlated with the areas of fitted peaks. It can be calculated that the contents of Ovs in TiO_2, TiO_2-1, TiO_2-2, and TiO_2-3 are 8.53%, 16.71%, 22.77%, and 30.59% (Table. S2), respectively. The Ov concentration in reduced TiO_2 shows a growing tendency with increasing lithium used, suggesting the concentration of Ov can be tuned effectively via the molten salt-lithium treatment method. XPS survey scan of reduced TiO_2 samples (Fig. S6) and K 2p, Cs 3d and Br 3d XPS of TiO_2-2 (Fig. S7) reveal that the samples are composed of Ti, O, and C without other impurities. The existence form of Li species on the surface of defective TiO_2-2 was discussed (Fig. S8 and S9) and the existence form of H species was analyzed (Fig. S10 and S11).

Raman spectroscopy was used to characterize the local structural properties of the TiO_2 samples (Fig. 2e). Pristine TiO_2 exhibited five Raman characteristic peaks at 145, 201, 403, 513, and 645 cm^{-1}, which can be indexed to Raman modes of E_g, E_g, B_{1g}, A_{1g}, and E_g, respectively
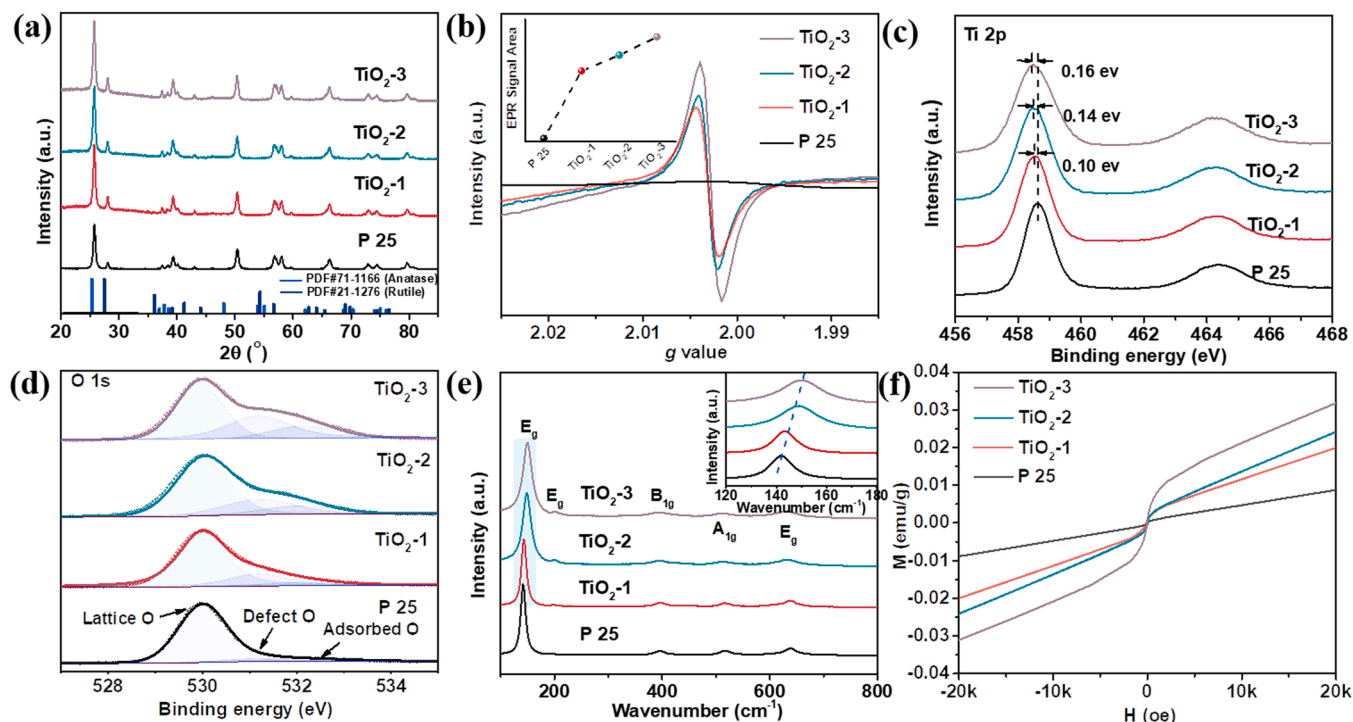
Fig. 2. (a) XRD patterns. (b) EPR spectra, inset is the EPR signal of differerent TiO_2 samples. (c) Ti 2p XPS. (d) O 1s XPS. (e) Raman spectra. (f) Magnetic field dependence of magnetization of different TiO_2 samples.
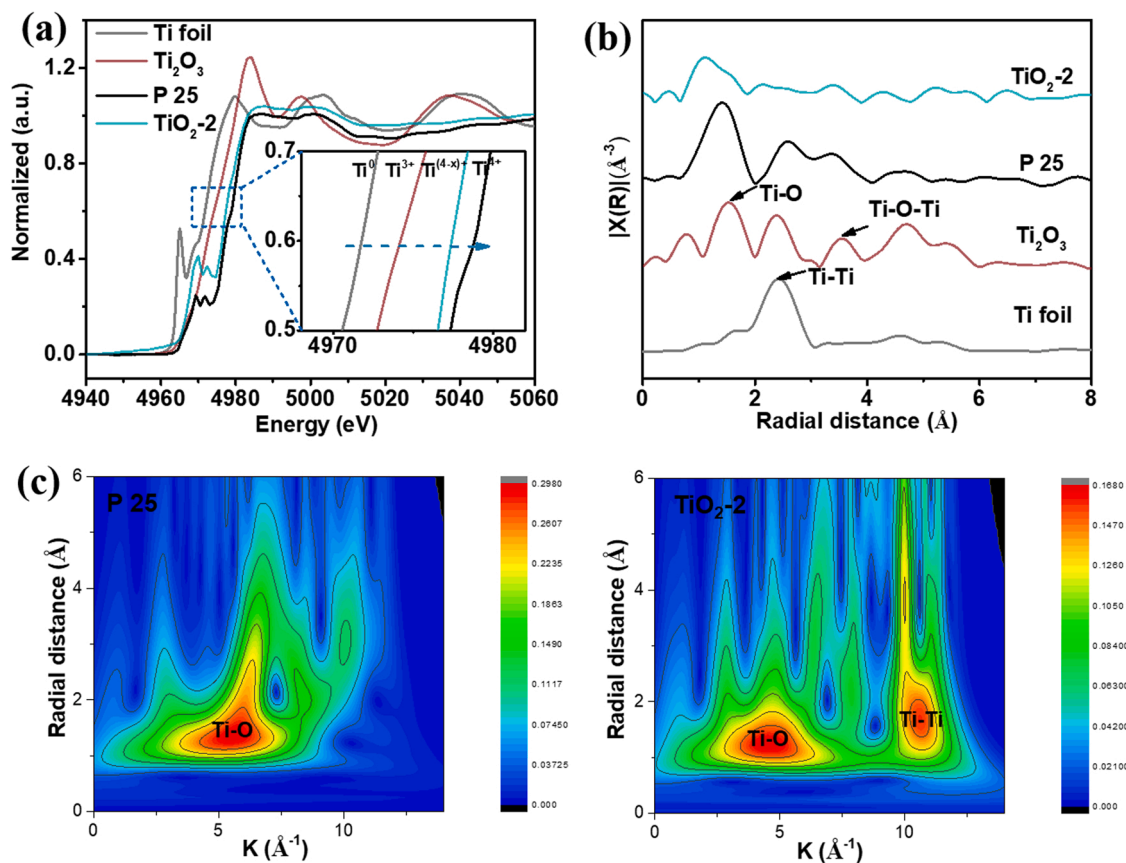

Fig. 3. (a) The XANES spectra (inset is the magnified image) and (b) Fourier-transformed Ti K-edge EXAFS spectra of pristine TiO_2, TiO_2-2, Ti_2O_3 and Ti metal. (c) The wavelet transforms for the k^3-weighted EXAFS signals of pristine TiO_2 and TiO_2-2 samples.

[35,36]. Impressively, after the molten salt-lithium treatment process, the main peak at 145 cm^{-1} demonstrated obvious blue-shift and peak broadening (inset of Fig. 2e). The change of the Raman peak can be ascribed to the non-stoichiometry on the TiO$_2$ surface, which is related to the deficiency of oxygen atoms. It can be explained that the amorphous structure accompanies the creation of Ov in the TiO$_2$ lattice. Note that the blue-shift effect becomes more evident with the growing content of Ovs, indicating the increase of crystal non-stoichiometry and disorder degree[37], which is consistent with HRTEM results. The existence of localized Ti^{3+} species can cause the ferromagnetic property of TiO$_2$. The field dependence of magnetization was tested to to index the reduction degree of TiO$_{2-x}$ samples (Fig. 2f). Reduced TiO$_2$ samples have a stronger magnetization with an increasing degree of reduction, accompanied by the gradual rise in Ti^{3+} concentration [16]. Moreover, the characterizations of molten salts (without lithium) treated TiO$_2$ were provided in Fig. S12-S15 for comparison.

X-ray absorption fine structure (XAFS) spectroscopy was further performed to illustrate the coordination environments of Ti in reduced TiO$_2$-2 samples. The normalized Ti K edge X-ray absorption near-edge structure (XANES) spectra (Fig. 3a) clearly show that Ti in the TiO$_2$-2 sample possesses the valence state between Ti^{3+} and Ti^{4+} (inset of Fig. 3a) [25,38], consistent with the XPS results. The Ti site distortion can be investigated by Fourier transformed extended XAFS (EXAFS) spectra (Fig. 3b). Both TiO$_2$ samples show two main peaks at ≈ 1.5 Å and ≈ 2.4 Å, corresponding to the first shell coordination of Ti-O and Ti-Ti bonds, respectively. It can be obtained that TiO$_2$-2 has decreased Ti-O bond intensity and decreased bond length, confirming the structural distortion in TiO$_2$-2 ascribed to the abundant Ov defects [39]. The EXAFS fitting curves of pristine TiO$_2$ and TiO$_2$-2 are exhibited in Fig. S16 and S17, respectively. The coordination numbers and bond lengths are listed in Table S3. The Fourier transformation of Ti K-edge EXAFS in

k-space and R space is provided in Fig. S18 and S19, respectively. The wavelet transforms (WT, Fig. 3c) profiles provide high resolution in both R and k spaces, and also highlight a shorter radial distance of Ti-O and an unsaturated coordination environment in TiO$_2$-2. The shrinkage of Ti-O distance is associated with significantly increased disorder degrees, which attributes to the absence of surface O atoms [40]. These results indicate that Ovs in TiO$_2$ lattice modulate the local electronic structure nearby Ov.

3.2. Photocatalytic RhB degradation performance

To verify the photocatalytic performance of TiO$_2$ with Ovs, RhB photocatalytic decomposition was carried out (Fig. 4a). Upon the irradiation of the visible light, TiO$_2$ with Ov illustrates obvious enhancement in photocatalytic performance compared with pristine TiO$_2$. Specifically, TiO$_2$-2 samples exhibit the best degradation ability, which could decompose ~90% RhB dye molecules within 60 min, whereas P 25 decomposes ~20% RhB within the same time. Moreover, the pseudo-first-order equation was collected to quantitatively reveal the degradation kinetics of RhB [41] (Fig. 4b). The kinetic constant K was calculated to be 0.0034, 0.0123, 0.0388 and 0.0280 min^{-1} for P 25, TiO$_2$-1, TiO$_2$-2 and TiO$_2$-3, respectively [41,42]. Amongst TiO$_2$ with different concentrations of Ov, TiO$_2$-2 exhibited the highest K value, which is ~11 times higher than pristine TiO$_2$. In order to illustrate photocatalytic degradation kinetics per surface area, the results were normalized with respect to surface area and summarized in Fig. 4c. The surface area normalized degradation kinetics constants of P 25, TiO$_2$-1, TiO$_2$-2 and TiO$_2$-3 are 0.0022, 0.0060, 0.0175 and 0.0098 min^{-1}, respectively. The results show that the excessive Ovs are detrimental to the dye degradation performance because they also act as the recombination centers for e$^-$ and h$^+$. The time evolution of UV-Vis absorbance spectra of RhB
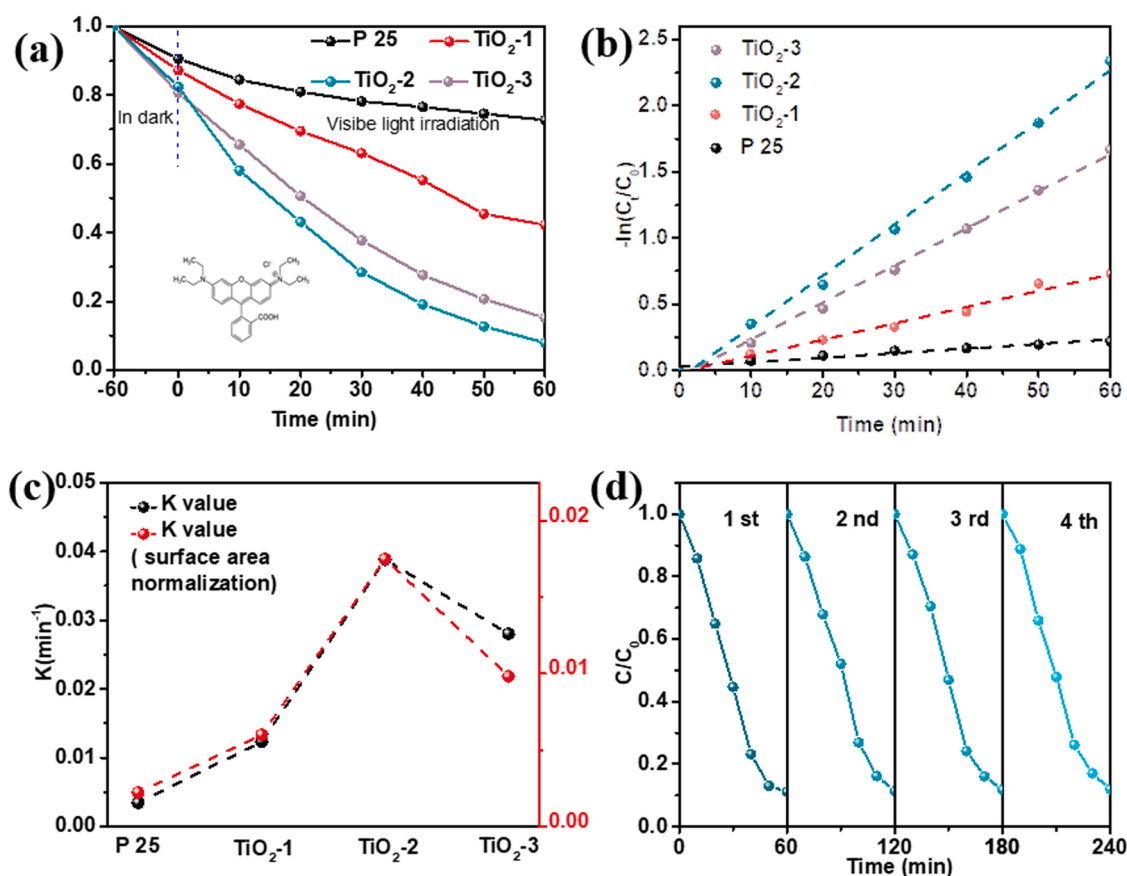

Fig. 4. (a) Photocatalytic degradation of RhB under visible-light irradiation. Inset is the molecular structure of RhB. (b) Pseudo first-order kinetic fitting. (c) Rate constants (K, min^{-1}) and surface area normalized K values. (d) Cycle performance of TiO$_2$-2 for photocatalytic RhB degradation.

dye under visible light irradiation indicates the de-ethylation process of the RhB molecules by TiO_2-2 nanoparticles (Fig. S20). The photocatalytic decomposition of RhB by TiO_2-2 was tested for four cycles (Fig. 4d), where almost no decay can be found during the cyclic test, proving the superior stability of TiO_2-2 catalyst. In order to investigate the thermal stability of Ov, TiO_2-2 nanoparticles were heated at 60 ℃ in the air for 5 days and subsequently utilized as photocatalysts (Fig. S21). It can be seen that the annealed TiO_2-2 still demonstrates excellent photocatalytic degradation property, proving the good thermal stability of TiO_2 with Ovs. The RhB adsorption properties of pristine TiO_2 and TiO_2-2 are fully discussed in the Supporting information (Fig. S22 and S23, Table S4 and S5). The possible reaction mechanisms on defective TiO_2 for photocatalytic RhB degradation is proposed and investigated (Fig. S24). The photocatalytic RhB degradation of TiO_2 photocatalysts under UV-Vis light irradiation is illustrated in Fig. S25 and S26.

3.3. Photocatalytic H_2 generation and photoelectrochemical performance

Further, photocatalytic H_2 production activity of TiO_2 samples was evaluated under 300 W Xenon lamp irradiation (Fig. 5a). The implantation of Ovs in TiO_2 can effectively promote the H_2 production rate. Typically, TiO_2-2 possesses the highest H_2 production rate. In comparison, P25, TiO_2-1 , TiO_2-2, and TiO_2-3 samples afford the H_2 production rate of 4.0, 25.8, 45.7, and 36.0 μmol g^{-1} h^{-1}, respectively. TiO_2-1, TiO_2-2, and TiO_2-3 demonstrate 5.5, 10.5, and 8.0 times higher H_2 production rates than that of pristine TiO_2, respectively. H_2 production rates per unit specific surface area were also calculated (Fig. 5b), which is 2.6, 12.5, 20.6, and 12.6 μmol m^{-2} h^{-1} for P25, TiO_2-1 , TiO_2-2, and TiO_2-3, respectively. TiO_2-3 with the largest surface area shows a lower H_2 production rate, verifying that excessive Ovs are unfavorable for photocatalytic hydrogen generation. The photocatalytic H_2 production stability of TiO_2-2 in Fig. 5c reveals no obvious decay during 4 cycles, suggesting its excellent photocatalytic stability. The photocatalytic H_2 generation performance of TiO_2 photocatalysts under UV-Vis light irradiation is illustrated in Fig. S27. It can been seen from electrochemical impedance spectroscopy (EIS) spectra (Fig. 5d) that TiO_2 with

gradient Ovs showed a much smaller radius than the pristine TiO_2 samples, indicative of a fast interfacial charge transfer property [41,43]. Photoelectrochemical measurements were performed to investigate the charge transfer and separation behaviors of TiO_2 (Fig. 5e). The photocurrent-time curves of TiO_2 show that TiO_2-2 yielded the highest photocurrent density, followed by TiO_2-3, TiO_2-1, and P25. The carrier densities of the samples can be obtained from the Mott-Schottky plots (Fig. S28), where TiO_2 with Ovs possesses higher carrier densities than pristine TiO_2. Photoluminescence (PL) spectra were carried out to study the photo-generated charge separation efficiency (Fig. S29) [44]. P25 and reduced TiO_2 samples demonstrate a similar PL spectra profile with a peak at 520 nm. Compared with P25, the PL emission intensity peak quenches after the introduction of Ovs, confirming an enhanced photo-generated carrier separation in TiO_2-Ov. Moreover, TiO_2-2 presents the lowest PL intensities, indicating that TiO_2-2 possesses the optimal photo-generated carrier separation efficiency with appropriate Ov concentration among reduced TiO_2 samples[45]. For further verification, time-resolved photoluminescence (TRPL) spectra were conducted to quantify the lifetime of photo-generated carriers (Fig. 5f). The average PL lifetimes of the samples were calculated with a biexponential decay function, which is 0.57, 0.84, 1.42, and 1.21 ns for P25, TiO_2-1, TiO_2-2, and TiO_2-3, respectively. The fitting parameters are summarized in Table. S6. The reduced TiO_2 samples have a longer average lifetime than pristine TiO_2, implying that proper concentration of Ovs could enhance the charge separation efficiency and prolong the lifetime of the excited electrons [46].

3.4. Density functional theory (DFT) calculations

In order to reveal the role of Ovs in enhancing the photocatalytic hydrogen evolution reaction (HER) performance of TiO_2 with Pt nanoparticles, we further performed density functional theory (DFT)+U calculations. DFT-calculated projected density of states (PDOS) for Ti 3d and O 2p orbitals are displayed in Fig. 6a. After the molten salt-lithium treatment, the generation of Ovs provides dispersed Ti^{3+} 3d energy levels, which locate between the conduction band minimum (CBM) and
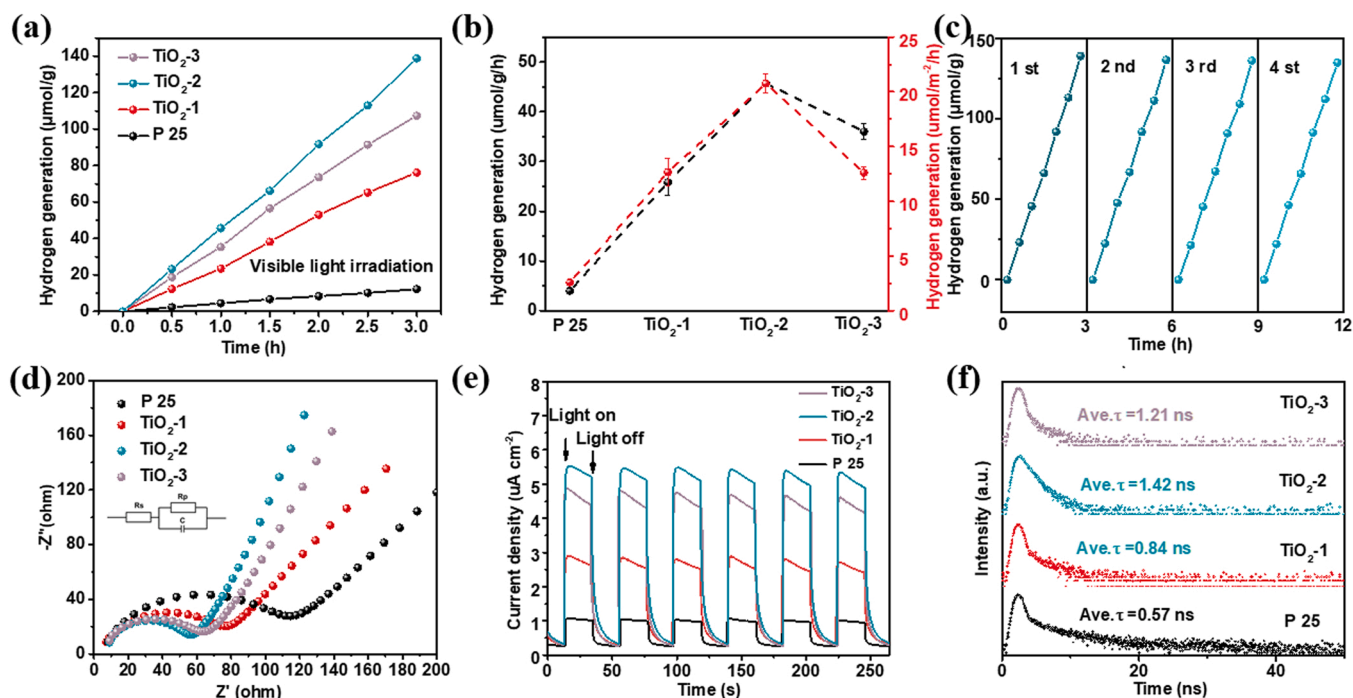

Fig. 5. (a) Photocatalytic H_2 generation curves over various TiO_2 samples under visible light irradiation. (b) Comparison of H_2 production rate and surface normalized H_2 production rate for different TiO_2 samples. (c) Cycling test of H_2 generation over TiO_2-2 sample. (d) EIS spectra. (e) Transient photocurrent spectra. (f) Time resolved PL spectra over various TiO_2 samples.
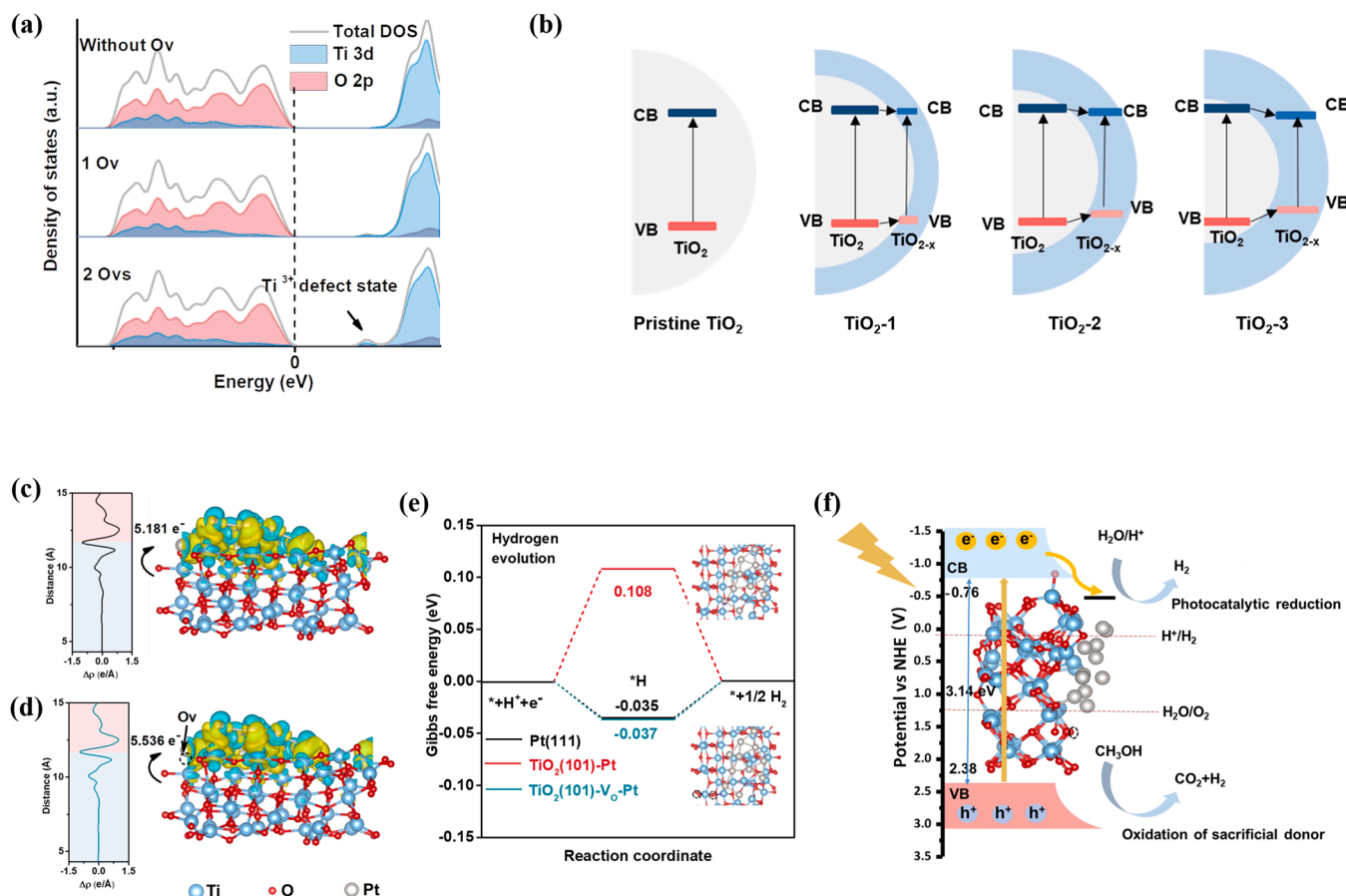
Fig. 6. (a) DFT-calculated projected density of states (PDOS) for Ti 3d and O 2p orbitals in a $2 \times 2 \times 2$ supercell of anatase TiO_2 containing 32 Ti and 64 O atoms without, with one, and with two Ovs, respectively. (b) The TiO_{2-x}/TiO_2 heterostructure showing photoinduced charge transfer routes in pristine TiO_2, TiO_2-1, TiO_2-2, and TiO_2-3, respectively. Charge density difference distribution (right) and planar-average charge density plot (left) between Pt and TiO_2 (101) (c) without Ov and (d) with Ov. Yellow and cyan clouds indicate charge gain and loss, respectively. (e) DFT-calculated Gibbs free energy diagram for hydrogen evolution reaction (HER) on TiO_2 (101)-Pt nanoparticle with and without Ov. HER on Pt (111) is calculated as a benchmark. (f) Schematic diagram of the photocatalytic process of TiO_2-Ov-Pt in promoting H_2 production.

valence band maximum (VBM). With the increase of Ov and Ti^{3+} concentrations, the band tail becomes broadened, resulting in the narrowed band gap of TiO_2. Due to this reason, the light absorption range of TiO_2 with Ovs can be extended to the visible region, and the light absorption ability is enhanced, generating an increased amount of photo-generated carriers. To gain deeper insights into the electronic structure change caused by Ovs, the band alignment was analyzed experimentally. Based on Tauc plot in Fig. S30, the bandgap (E_g) of P25, TiO_2-1, TiO_2-2 and TiO_2-3 can be estimated to be 3.28 eV, 3.22 eV, 3.14 eV and 3.07 eV, respectively. The valence band (VB) XPS in Fig. S31 reveals that the VBM of P25, TiO_2-1, TiO_2-2 and TiO_2-3 are 2.45 eV, 2.42 eV, 2.38 eV and 2.33 eV, respectively. CBM can be calculated by the equation CBM = VBM- E_g, to be -0.83 eV, -0.80 eV, -0.76 eV and -0.74 eV for P25, TiO_2-1, TiO_2-2 and TiO_2-3, respectively. The obtained band structure is depicted in Fig. S32. In order to understand charge transport and mobility properties of the different TiO_2-Ov samples, TiO_2/TiO_{2-x} heterostructure is proposed to discuss the charge separation mechanism. As illustrated in Fig. 6b, the implantation of Ovs is accompanied by TiO_2 transforming to the amorphous TiO_{2-x} shell at the outer layer of the nanoparticle, forming the TiO_2/TiO_{2-x} heterostructure. With the increase of the Ov concentration, the thickness of TiO_{2-x} increased. Further, the relative positions of the VB and CB in the electronic band diagram of TiO_2/TiO_{2-x} is depicted. A charge separation mechanism exists at the TiO_2/TiO_{2-x} interface by charge transfer from TiO_2 to TiO_{2-x}. Once solar light is absorbed, photogenerated electrons and holes in the TiO_2 CB and VB can respectively transfer to the CB and VB in

TiO_{2-x}, thus accelerating charge separation efficiency. However, the excess Ovs are detrimental to the photocatalytic performance, because they would block the charge separation and transfer to TiO_2 surfaces resulted from the destroyed atomic structures. In addition, the increased thickness of TiO_{2-x} shell extends the vertical migration distance of charge carriers from the interface to the surface, which is unfavorable to the photocatalytic activity. This can explain why TiO_2-3 shows attenuation in photocatalytic performance. The calculated numbers of Bader charge transfer [47] from TiO_2 to Pt and the corresponding planar-average charge density are marked in the Fig. 6c. Compared with TiO_2-Pt, TiO_2-Ov-Pt (Fig. 6d) reveals a more negative charge. These results confirm the strong correlation between TiO_2-Ov and Pt. It can be speculated that Ovs regulate the electron distribution and may strongly affect the binding energies of absorbates. In theory, an ideal HER catalyst should bind the hydrogen neither too strong nor too weak to increase the kinetics of Volmer and Tafel/Heyrovky steps simultaneously, i.e., to exhibit close-to-zero hydrogen adsorption free energy $\Delta G(*H)$ [48]. The structure models of TiO_2-Pt and TiO_2-Ov-Pt are displayed in the inset of Fig. 6e. As a benchmark, the $\Delta G(*H)$ for Pt (111) is calculated to be -0.035 eV (Fig. 6e). All the calculations were conducted on the (101) surface of anatase TiO_2. The calculation results show that TiO_2 (101)-Pt exhibits $\Delta G(*H)$ value of 0.108 eV, while for TiO_2-Ov (101)-Pt, the adsorbed hydrogen can interact with both Pt and Ov, leading to stabilized *H intermediates with $\Delta G(*H)$ of -0.037 eV, very close to that for Pt (111), indicating that Ovs can enhance the HER kinetics toward the optimum. Considering the above analyses, an overall

mechanism is proposed to understand the process of photocatalytic H_2 production over TiO_2-2-Pt. As illustrated in Fig. 6f, upon irradiation of visible light, the TiO_2-2-Pt absorbs photon energy to generate photoinduced e^- and h^+, then e^- and h^+ transport to the surface of TiO_2-2. Afterward, e^- transfers to Pt nanoparticle due to the Schottky junction. Then, e^- and h^+ react with adsorbed molecules, respectively. H_2O/H^+ is reduced by e^- to produce H_2, while methanol as a sacrifice agent is oxidized by h^+ to produce CO_2 and H_2 [49]. The remarkable photocatalytic activity can be ascribed to the following mechanism: (i) The implantation of Ovs changes the band structure. The narrowed bandgap expands the absorption region to the visible region, which increases the number of e^- and h^+. (ii) Ov can enhance the HER kinetics, electron-rich Pt induced by Ov is responsible for the enhanced intrinsic activity of photocatalysts, the stabilized *H intermediates exhibit $\Delta G(*H)$ of -0.037 eV. (iii) The enhanced surface area provides more photocatalytic active sites and facilitates the surface photocatalytic reduction reaction kinetics by rapidly transferring the reactant and product. At the same time, it can effectively shorten the electron diffusion paths. Ovs and enlarged surface area jointly improve the efficiency of all the key photocatalytic steps, resulting in more optimized η_{abs}, η_{cs} and η_{redox} to achieve excellent photocatalytic H_2 production performance.

4. Conclusions

In conclusion, a novel facile and controllable molten salt-lithium method was developed to simultaneously fulfill gradient modulation of Ov and surface microstructure in TiO_2 for efficient photocatalysis. The ternary molten salt system provided a unique liquid environment for the formation of Ov in TiO_2 at low temperature. Meanwhile, the etching effect of the molten salt-lithium mixture enlarged the surface area of TiO_2. Photocatalytic RhB degradation kinetic of TiO_2-2 exhibits ~11 times higher than pristine TiO_2, and photocatalytic H_2 generation of TiO_2-2 demonstrates ~10-fold higher than pristine TiO_2 under visible light irradiation. Moreover, Ovs and enlarged surface area play synergistic roles in enhancing the photocatalytic performance. The reduced bandgap caused by the Ov generates an enhanced number of photogenerated carriers, which improves the hydrogen evolution reaction kinetics through adsorbed hydrogen interacting with Ov. Furthermore, the significantly enlarged surface area offers more active sites to adsorb reaction molecules. Experimental results also verify that excessive Ovs are unfavorable for photocatalysis. This study may provide a promising approach to precisely tailor Ovs and surface morphology to boost the photocatalytic activity and highlights the significance of simultaneous optimization the efficiency of photocatalytic processes.

CRediT authorship contribution statement

Di Zu: Conceptualization, Data curation, Investigation, Writing – original draft. **Yiran Ying:** Theoretical calculation, Writing. **Zhihang Xu:** Characterization. **Liqi Bai:** Characterization. **Gao Chen:** Investigation, Data curation. **Safayet Ahmed:** Review & editing. **Zezhou Lin:** Visualization. **Ye Zhu:** Characterization. **Ahmed Mortuza Saleque:** Review & editing. **Sixuan She:** Investigation. **Molly Mengjung Li:** Investigation. **Md. Nahian Al Subri Ivan:** Investigation **Hui Wu:** Review & editing, Supervision. **Yuen Hong Tsang:** Funding acquisition, Review & editing, Supervision. **Haitao Huang:** Funding acquisition, Review & editing, Supervision.

Declaration of Competing Interest

The authors declare that they have no known competing financial interests or personal relationships that could have appeared to influence the work reported in this paper.

Data availability

Data will be made available on request.

Appendix A. Supporting information

Supplementary data associated with this article can be found in the online version at doi:10.1016/j.apcatb.2023.122494.

References

[1] D.M. Zhao, Y.Q. Wang, C.L. Dong, Y.C. Huang, J. Chen, F. Xue, S.H. Shen, L.J. Guo, Boron-doped nitrogen-deficient carbon nitride-based Z-scheme heterostructures for photocatalytic overall water splitting, Nat. Energy 6 (2021) 388–397.

[2] D.W. Wakerley, M.F. Kuehnel, K.L. Orchard, K.H. Ly, T.E. Rosser, E. Reisner, Solar-driven reforming of lignocellulose to H_2 with a CdS/CdOx photocatalyst, Nat. Energy 2 (2017).

[3] Z. Tian, C. Han, Y. Zhao, W. Dai, X. Lian, Y. Wang, Y. Zheng, Y. Shi, X. Pan, Z. Huang, H. Li, W. Chen, Efficient photocatalytic hydrogen peroxide generation coupled with selective benzylamine oxidation over defective ZrS_3 nanobelts, Nat. Commun. 12 (2021) 2039.

[4] K.H. Kim, C.W. Choi, S. Choung, Y. Cho, S. Kim, C. Oh, K.S. Lee, C.L. Lee, K. Zhang, J.W. Han, S.Y. Choi, J.H. Park, Continuous oxygen vacancy gradient in TiO_2 photoelectrodes by a photoelectrochemical-driven "Self-Purification" Process, Adv. Energy Mater. 12 (2022).

[5] Y.X. Tan, Z.M. Chai, B.H. Wang, S. Tian, X.X. Deng, Z.J. Bai, L. Chen, S. Shen, J.K. Guo, M.Q. Cai, C.T. Au, S.F. Yin, Boosted photocatalytic oxidation of toluene into benzaldehyde on $CdIn_2S_4$-CdS: synergetic effect of compact heterojunction and S-vacancy, ACS Catal. 11 (2021) 2492–2503.

[6] B. Zhao, Y. Wang, X. Yao, D. Chen, M. Fan, Z. Jin, Q. He, Photocatalysis-mediated drug-free sustainable cancer therapy using nanocatalyst, Nat. Commun. 12 (2021) 1345.

[7] Y. Xu, M. Fan, W. Yang, Y. Xiao, L. Zeng, X. Wu, Q. Xu, C. Su, Q. He, Homogeneous carbon/potassium-incorporation strategy for synthesizing red polymeric carbon nitride capable of near-infrared photocatalytic H_2 production, Adv. Mater. 33 (2021), e2101455.

[8] Z. Wang, C. Li, K. Domen, Recent developments in heterogeneous photocatalysts for solar-driven overall water splitting, Chem. Soc. Rev. 48 (2019) 2109–2125.

[9] N. Zhang, A. Jalil, D. Wu, S. Chen, Y. Liu, C. Gao, W. Ye, Z. Qi, H. Ju, C. Wang, X. Wu, L. Song, J. Zhu, Y. Xiong, Refining defect states in $W_{18}O_{49}$ by Mo doping: a strategy for tuning N_2 activation towards solar-driven nitrogen fixation, J. Am. Chem. Soc. 140 (2018) 9434–9443.

[10] J. Xu, Z. Ju, W. Zhang, Y. Pan, J. Zhu, J. Mao, X. Zheng, H. Fu, M. Yuan, H. Chen, R. Li, Efficient infrared-light-driven CO_2 reduction over ultrathin metallic Ni-doped CoS_2 nanosheets, Angew. Chem. 60 (2021) 8705–8709.

[11] X.Q. Hao, J. Zhou, Z.W. Cui, Y.C. Wang, Y. Wang, Z.G. Zou, Zn-vacancy mediated electron-hole separation in $ZnS/g-C_3N_4$ heterojunction for efficient visible-light photocatalytic hydrogen production, Appl. Catal. B Environ. 229 (2018) 41–51.

[12] S.W. Cao, B.J. Shen, T. Tong, J.W. Fu, J.G. Yu, 2D/2D heterojunction of ultrathin $MXene/Bi_2WO_6$ nanosheets for improved photocatalytic CO_2 reduction, Adv. Funct. Mater. 28 (2018).

[13] X. Du, Y. Huang, X. Pan, B. Han, Y. Su, Q. Jiang, M. Li, H. Tang, G. Li, B. Qiao, Size-dependent strong metal-support interaction in TiO_2 supported Au nanocatalysts, Nat. Commun. 11 (2020) 5811.

[14] J.G. Hou, S.Y. Cao, Y.Q. Sun, Y.Z. Wu, F. Liang, Z.S. Lin, L.C. Sun, Atomically thin mesoporous In_2O_3-x/In_2S_3 lateral heterostructures enabling robust broadband-light photo-electrochemical water splitting, Adv. Energy Mater. 8 (2018).

[15] B. Li, Y. Zhang, R. Du, L. Gan, X. Yu, Synthesis of Bi_2S_3-Au dumbbell heteronanostructures with enhanced photocatalytic and photoresponse properties, Langmuir 32 (2016) 11639–11645.

[16] L. Pan, M. Ai, C. Huang, L. Yin, X. Liu, R. Zhang, S. Wang, Z. Jiang, X. Zhang, J. J. Zou, W. Mi, Manipulating spin polarization of titanium dioxide for efficient photocatalysis, Nat. Commun. 11 (2020) 418.

[17] Z. Geng, X. Kong, W. Chen, H. Su, Y. Liu, F. Cai, G. Wang, J. Zeng, Oxygen vacancies in ZnO nanosheets enhance CO_2 electrochemical reduction to CO, Angew. Chem. 57 (2018) 6054–6059.

[18] L. Hao, H.W. Huang, Y.H. Zhang, T.Y. Ma, Oxygen vacant semiconductor photocatalysts, Adv. Funct. Mater. 31 (2021).

[19] J. Kang, Y. Zhang, Z. Chai, X. Qiu, X. Cao, P. Zhang, G. Teobaldi, L.M. Liu, L. Guo, Amorphous domains in black titanium dioxide, Adv. Mater. 33 (2021), e2100407.

[20] X. Chen, L. Liu, P.Y. Yu, S.S. Mao, Increasing solar absorption for photocatalysis with black hydrogenated titanium dioxide nanocrystals, Science 331 (2011) 746–750.

[21] G. Ou, Y. Xu, B. Wen, R. Lin, B. Ge, Y. Tang, Y. Liang, C. Yang, K. Huang, D. Zu, R. Yu, W. Chen, J. Li, H. Wu, L.M. Liu, Y. Li, Tuning defects in oxides at room temperature by lithium reduction, Nat. Commun. 9 (2018) 1302.

[22] M. Xiao, L. Zhang, B. Luo, M. Lyu, Z. Wang, H. Huang, S. Wang, A. Du, L. Wang, Molten-salt-mediated synthesis of an atomic nickel Co-catalyst on TiO₂ for improved photocatalytic H₂ evolution, Angew. Chem. 59 (2020) 7230–7234.

[23] P. Urbankowski, B. Anasori, T. Makaryan, D. Er, S. Kota, P.L. Walsh, M. Zhao, V. B. Shenoy, M.W. Barsoum, Y. Gogotsi, Synthesis of two-dimensional titanium nitride Ti₄N₃ (MXene), Nanoscale 8 (2016) 11385–11391.

[24] B. Ravel, M. Newville, ATHENA, ARTEMIS, HEPHAESTUS: data analysis for X-ray absorption spectroscopy using IFEFFIT, J. Synchrotron Radiat. 12 (2005) 537–541.

[25] A. Janotti, J.B. Varley, P. Rinke, N. Umezawa, G. Kresse, C.G. Van, de Walle, Hybrid functional studies of the oxygen vacancy in TiO₂, Phys. Rev. B 81 (2010).

[26] F. Yang, H.Z. Li, K. Pan, S.J. Wang, H.P. Sun, Y. Xie, Y.C. Xu, J.X. Wu, W. Zhou, Engineering surface N-vacancy defects of ultrathin mesoporous carbon nitride nanosheets as efficient visible-light-driven photocatalysts, Sol. PRL 5 (2021).

[27] D. Knez, G. Drazic, S.K. Chaluvadi, P. Orgiani, S. Fabris, G. Panaccione, G. Rossi, R. Ciancio, Unveiling oxygen vacancy superstructures in reduced anatase thin films, Nano Lett. 20 (2020) 6444–6451.

[28] Z. Li, C. Zhou, J. Hua, X. Hong, C. Sun, H.W. Li, X. Xu, L. Mai, Engineering oxygen vacancies in a polysulfide-blocking layer with enhanced catalytic ability, Adv. Mater. 32 (2020), e1907444.

[29] S. Liu, L. Han, Y. Duan, S. Asahina, O. Terasaki, Y. Cao, B. Liu, L. Ma, J. Zhang, S. Che, Synthesis of chiral TiO₂ nanofibre with electron transition-based optical activity, Nat. Commun. 3 (2012) 1215.

[30] M. Altomare, N.T. Nguyen, S. Hejazi, P. Schmuki, A. Cocatalytic, Electron-transfer cascade site-selectively placed on TiO₂ nanotubes yields enhanced photocatalytic H₂ evolution, Adv. Funct. Mater. 28 (2018).

[31] H. Yu, J. Li, Y. Zhang, S. Yang, K. Han, F. Dong, T. Ma, H. Huang, Three-in-one oxygen vacancies: whole visible-spectrum absorption, efficient charge separation, and surface site activation for robust CO₂ photoreduction, Angew. Chem. 58 (2019) 3880–3884.

[32] R. Li, X. Ma, J. Li, J. Cao, H. Gao, T. Li, X. Zhang, L. Wang, Q. Zhang, G. Wang, C. Hou, Y. Li, T. Palacios, Y. Lin, H. Wang, X. Ling, Flexible and high-performance electrochromic devices enabled by self-assembled 2D TiO₂/MXene heterostructures, Nat. Commun. 12 (2021) 1587.

[33] Y. Zhao, Y. Zhao, R. Shi, B. Wang, G.I.N. Waterhouse, L.Z. Wu, C.H. Tung, T. Zhang, Tuning Oxygen Vacancies in Ultrathin TiO₂ Nanosheets to Boost Photocatalytic Nitrogen Fixation up to 700 nm, Adv. Mater. 31 (2019), e1806482.

[34] J. Zheng, Y. Lyu, R. Wang, C. Xie, H. Zhou, S.P. Jiang, S. Wang, Crystalline TiO₂ protective layer with graded oxygen defects for efficient and stable silicon-based photocathode, Nat. Commun. 9 (2018) 3572.

[35] I. Alessandri, Enhancing Raman scattering without plasmons: unprecedented sensitivity achieved by TiO₂ shell-based resonators, J. Am. Chem. Soc. 135 (2013) 5541–5544.

[36] E. Han, K. Vijayarangamuthu, J.S. Youn, Y.K. Park, S.C. Jung, K.J. Jeon, Degussa P25 TiO₂ modified with H₂O₂ under microwave treatment to enhance photocatalytic properties, Catal. Today 303 (2018) 305–312.

[37] Z. Sun, R. Huo, C. Choi, S. Hong, T.-S. Wu, J. Qiu, C. Yan, Z. Han, Y. Liu, Y.-L. Soo, Y. Jung, Oxygen vacancy enables electrochemical N₂ fixation over WO₃ with tailored structure, Nano Energy 62 (2019) 869–875.

[38] L. Bai, H. Huang, S. Zhang, L. Hao, Z. Zhang, H. Li, L. Sun, L. Guo, H. Huang, Y. Zhang, Photocatalysis-Assisted Co₃O₄/g-C₃N₄ p-n Junction All-Solid-State Supercapacitors: A Bridge between Energy Storage and Photocatalysis, Adv. Sci. 7 (2020), 2001939.

[39] V.K. Paidi, B.H. Lee, D. Ahn, K.J. Kim, Y. Kim, T. Hyeon, K.S. Lee, Oxygen-vacancy-driven orbital reconstruction at the surface of TiO₂ core-shell nanostructures, Nano Lett. 21 (2021) 7953–7959.

[40] K. Chu, Y. Luo, P. Shen, X. Li, Q. Li, Y. Guo, Unveiling the Synergy of O-Vacancy and Heterostructure over MoO₃₋ₓ/MXene for N₂ Electroreduction to NH₃, Adv. Energy Mater. 12 (2021).

[41] J.R. Wu, W.W. Wang, Y. Tian, C.X. Song, H. Qiu, H. Xue, Piezotronic effect boosted photocatalytic performance of heterostructured BaTiO₃/TiO₂ nanofibers for degradation of organic pollutants, Nano Energy 77 (2020).

[42] J. Wang, Y. Xia, H.Y. Zhao, G.F. Wang, L. Xiang, J.L. Xu, S. Komarneni, Oxygen defects-mediated Z-scheme charge separation in g-C₃N₄/ZnO photocatalysts for enhanced visible-light degradation of 4-chlorophenol and hydrogen evolution, Appl. Catal. B Environ. 206 (2017) 406–416.

[43] R. Si, X. Xie, T. Li, J. Zheng, C. Cheng, S. Huang, C. Wang, TiO₂/(K,Na)NbO₃ nanocomposite for boosting humidity-sensing performances, ACS Sens. 5 (2020) 1345–1353.

[44] S. Wang, B.Y. Guan, X. Wang, X.W.D. Lou, Formation of Hierarchical Co₉S₈@ ZnIn₂S₄ Heterostructured Cages as an Efficient Photocatalyst for Hydrogen Evolution, J. Am. Chem. Soc. 140 (2018) 15145–15148.

[45] X. Zhang, P.J. Ma, C. Wang, L.Y. Gan, X.J. Chen, P. Zhang, Y. Wang, H. Li, L. H. Wang, X.Y. Zhou, K. Zheng, Unraveling the dual defect sites in graphite carbon nitride for ultra-high photocatalytic H₂O₂ evolution, Energ. Environ. Sci. 15 (2022) 830–842.

[46] X.L. Zhao, S. Chen, H.J. Yin, S.Y. Jiang, K. Zhao, J. Kang, P.F. Liu, L.X. Jiang, Z.J. Zhu, D.D. Cui, P.R. Liu, X.J. Han, H.G. Yang, H.J. Zhao, Perovskite Microcrystals with Intercalated Monolayer MoS₂ Nanosheets as Advanced Photocatalyst for Solar-Powered Hydrogen Generation, Matter, 3 (2020) 935–949.

[47] W. Tang, E. Sanville, G. Henkelman, A grid-based Bader analysis algorithm without lattice bias, J. Phys.: Condens. Matter 21 (2009), 084204.

[48] Z.W. Seh, J. Kibsgaard, C.F. Dickens, I. Chorkendorff, J.K. Norskov, T.F. Jaramillo, Combining theory and experiment in electrocatalysis: Insights into materials design, Science 355 (2017) eaad4998.

[49] P.V. Kamat, S. Jin, Semiconductor photocatalysis: "Tell us the complete story!", ACS Energy Lett. 3 (2018) 622–623.